Supporting Information (SI Appendix): Low-gradient, single-threaded rivers prior to greening of the continents

A. Geological Context and Regional Background

The "Torridonian Sandstone" is an informal stratigraphic name used to refer to the entire suite of Middle to Upper Proterozoic rocks exposed in the northwest highlands of Scotland, UK, comprising arkoses and subfeldspathic arenites, with occasional conglomerate and very minor shale horizons (1–4). They are internationally recognized as a classic type-example of Precambrian fluvial sedimentation. The rocks are exposed in a belt 20–30 km wide and more than 200 km long in northern Scotland (Fig. 1), lying underneath and cropping out in a window north of the trace of the regionally-significant Moine Thrust. They were deposited on top of Archean to Lower Proterozoic 'Lewisian' metamorphic basement over an unconformity surface with considerable erosional relief. Stratigraphically, the Torridonian succession has been divided into three groups (5): the Middle Proterozoic Stoer Group, the Sleat Group (which is mostly exposed on the Isle of Skye, Scotland, and whose relationship with the Stoer Group is enigmatic), and the Torridonian Group, which sits on an angular unconformity over the Stoer Group, but conformably overlies the Sleat Group where present. The data in this study solely refers to sedimentary strata of the Torridonian Group, which are Upper Proterozoic in age (4, 6). Diagenetic phosphate concretions in the lowest Torridonian Group yielded a whole rock Rb-Sr age of 994 ± 48 Ma and a Pb-Pb age of 951 ± 120 Ma (6, 7); these units unconformably overlie the well-studied Stac-Fada member of the Stoer Group, dated to 1177 ± 5 Ma (8), which constrains the onset of Torridonian sedimentation to early Neoproterozoic time. The Torridonian Group is unconformably capped by Cambrian quartzite (4).

www.pnas.org/cgi/doi/10.1073/pnas.1901642116

Three variables were measured in the field: a) set thickness, which is the thickness of the sedimentary package bounded by successive erosional boundaries (Fig. 2G), b) median grain size, which was estimated using scaled photographs and grain size card (Fig. 2H), and c) paleo-flow direction (Fig. 1C), which was estimated from the measured dip and dip direction of planar cross-bedding or the trend and plunge of the center of the trough cross beds, together with a correction for the dip and dip direction of the depositional bedding at each location (9).

B. Variability-dominated preservation of river dune evolution

Cross-stratified sets are depositional units formed by the migration of bedforms, and geometry of sets is controlled by the size of the formative bedforms, net aggradation rate, and the bedform celerity (10–13). Although the preservation of formsets can be common (13), especially when the local aggradation rates exceed bedform celerity, field evidence suggests that cross-stratification in the Torridonian Sandstone was a result of variable scours from migrating bedforms (Fig. S9). The empirical scaling relationship between cross-sets and formative bedform heights used in our study is based on an exact theory developed by Paola and Borgman (11) for the formation of cross-sets due to migrating bedforms under no net aggradation. They showed that the probability distribution of set thicknesses is given by the following one-parameter equation:

$$f(d_{st}) = \frac{a e^{-a d_{st}}\left(e^{-a d_{st}} + a d_{st} - 1\right)}{\left(1 - e^{-a d_{st}}\right)^2} \qquad \text{(S1)}$$

in which $d_{st} > 0$ is the set thickness, and a is the parameter of the distribution and is equal to $2/\beta$, where β is the scale parameter of the Gamma distribution describing the formative bedform heights. The theoretical coefficient of variation of the distribution of set thicknesses is 0.88 (11).

The aforementioned distribution can be fit to the data when set thicknesses are measured at random spanning the entire set. Further, Bridge (14) demonstrated that the scaling relationship between cross-set thickness and mean bedform heights, and equation (S1) can be applied when the measured coefficient of variation of set thickness within a single set was 0.88 ± 0.3.

Measuring the set thickness across a complete set can be difficult in the field owing to the limited lateral exposure of outcrops; however, where near-complete exposure of sets were available in the field, the measured coefficient of variation of set thickness was within the bounds suggested by Bridge (14), and the theoretical density function of equation (S1) provided a reasonable description of the measured density of set thicknesses across the three stratigraphic intervals (Fig. S9). This observation is consistent with the inference that the bed sets were created by variables scours of migrating fluvial bedforms. Further, the estimated mean set thickness of these individual, near-complete sets was similar to the global mean of the set thickness within each stratigraphic interval. Thus, we used the global mean of set thickness within each stratigraphic interval for estimating the formative bedform heights.

C. Comparison of flow depth estimates using different scaling relationships

Several studies have demonstrated that bedform heights can be related to their formative flow depth, transport stage, grain size, shear stress and other parameters of the flow conditions (15); however, not all these relationships can be used within a stratigraphic framework owing to the difficulty of robust inversion of key parameters of flow conditions. In this study, we used the h_d-H scaling relation reported by Bradley and Venditti (15). Other commonly used scaling relationships to invert for H include a relation provided by Leclair and Bridge (10), which builds on the work of Yalin (16), where the ratio of H to h_d was constrained to lie within a range of 6 to 10 with a mean of 8. Allen (17) provided a different formula for estimating H given by:

$$H = 11.62(h_d)^{0.84} \quad \text{(S2)}$$

where all quantities are in m. Estimating the formative flow depths from the aforementioned methods did not change our results significantly (Fig. S12). We used the method presented in Bradley and Venditti (15) because the uncertainty in the prediction of H was constrained, which allowed us to propagate this uncertainty into the estimation of slope and aspect ratio of channels through Monte Carlo sampling.

D. Bedform stability diagrams

Several decades of experimental and field research resulted in the formulation of a graphical framework that represents the conditions of flow, sediment transport, and fluid properties necessary for the stable existence of various bed states in alluvial rivers (e.g., ripples, dunes, lower plane bed, upper plane bed, antidunes)(18–23). Dimensional analysis indicates that at least three independent dimensionless numbers are required to characterize the stability of bedform states, and the commonly used dimensionless numbers are Froude number (Fr, which determines the state of the flow), Shields parameter (τ^*, describes the intensity of sediment transport), and particle Reynolds number (Re_p, that accounts for grain size and fluid viscosity), given by:

$$Fr = \frac{U}{\sqrt{gH}} \quad \text{(S3a)}$$

$$\tau^* = \frac{\tau_b}{(\rho_s - \rho) g D_{50}} \quad \text{(S3b)}$$

$$Re_p = \frac{\sqrt{RgD_{50}^3}}{\nu} \text{ (S3c)}$$

where U is the depth-averaged flow velocity, g is the gravitational acceleration, H is the flow depth, τ_b is the bed shear stress approximated as ρgHS for steady, uniform flow conditions, ρ_s is the density of sediment, ρ is the density of fluid, D_{50} is the median grain-size, R is the submerged specific density of sediment, and ν is the kinematic viscosity of the fluid, which is temperature-dependent. For subcritical flows, the bedform stability diagram is independent of the Froude number and can be expressed in terms of the Shields stress and the particle Reynolds number. We used the bedform stability diagram of Lamb et al. (20) to constrain the dimensionless bed shear stress in this study. Lamb et al. (20) compiled existing field and experimental studies, and constructed a comprehensive bedform stability diagram that spans a large range in particle Reynolds numbers. Using this compilation, they delineated the boundaries between different bed states (Fig. S10A). We estimated the particle Reynolds number for our stratigraphic sampling intervals using the measured median grain-size (Fig. 2H), and by assuming a kinematic viscosity of water of 10^{-6} m^2/s. Froude number, which is needed for evaluating the stability of planform morphology (Fig. 3D), was estimated for Torridonian rivers using equation (S3a).

E. Data compilation of Proterozoic cross-set thickness

We compiled cross-set thickness across 10 fluvial formations in the Proterozoic Eon (24–30). We chose a representative global sample that spanned Paleoproterozoic to Neoproterozoic deposits and restricted our compilation to studies that made extensive measurements of cross-set thickness to ensure that the measurements were a representative sample of each formation. Median grain-size measurements were not directly reported in previous studies; however, they noted that the cross-sets were composed of medium-to-coarse sand. In some cases, we corroborated these estimates using the reported microphotographs of the sandstone units. For each formation, we estimated paleoslope by taking a conservative approach, where we assumed the median grain-size to be uniformly distributed and bound by 0.5 to 1.5 mm for Monte Carlo sampling (equations 2, 3 in *Materials and Methods*). Similar to the paleohydraulic analyses of the Torridonian Group, we estimated the flow depth from H-h_d scaling relation (equation 1 in *Materials and Methods*) and we used both the bedform stability diagram and modern empirical scaling relationships to estimate paleoslope through Monte Carlo sampling (Fig. 4 in main text).

F. Previous estimates of paleogradients of Proterozoic rivers

A range of studies spanning three Paleoproterozoic formations, two Mesoproterozoic formations and multiple Neoproterozoic formations across four continents have suggested that gradients of Proterozoic rivers were steeper than that observed in post-Cambrian systems (24, 25, 27, 31–36). These studies estimated gradients using measured cross-stratal thickness and empirical relationships based on width-depth scaling and discharge-width scaling of modern rivers. In particular, all these studies used empirical relationships that relate paleoslope to the width-depth ratio of flows and percentage of silt and clay in the channel perimeter (37, 38). Width-depth ratios were also empirically related to the percentage of silt and clay in the channel perimeter, which was equated to 5% on the basis of the *a priori* assumption that Proterozoic rivers were large bedload systems that were devoid of any cohesive bank strength. These results yielded average slopes for Proterozoic rivers that spanned 4×10^{-3} to 4×10^{-2}. These observations suggest that Proterozoic rivers resided in the natural depositional slope gap between modern alluvial fans and rivers — a consequence of hydrodynamic differences between flows (Froude-supercritical vs Froude-subcritical) that shape alluvial fans and rivers, respectively (39).

Consensus on the cause of steep Proterozoic fluvial gradients is currently lacking, and previous studies have attributed this inference to unique combination of weathering regime in the Proterozoic Eon and lack of vegetation (25), tectono-sedimentary history of basin evolution in combination with rigorous climate (34), and production of argillaceous sediment under hyper-greenhouse atmospheric conditions, which enabled temporary storage of this sediment to sustain steep slopes (27). It has also been noted that none of these mechanisms provide a unifying explanation for the steep fluvial gradients inferred in Proterozoic deposits worldwide, given that mud preservation in most Proterozoic fluvial systems is negligible (24). The lack of consensus on the cause of steep gradients across Proterozoic rivers together with the geodynamical implications indicated in our study suggest that steep super-continental-scale Proterozoic rivers that resided in the natural depositional slope gap between alluvial fans and alluvial rivers were unlikely to have existed. Moreover, the inferred steep paleoslopes from previous studies are inconsistent with the observation of ubiquitous cross-stratification throughout the Proterozoic eon, and also with the inference that these rivers represented predominantly bedload systems.

G. Data compilation of modern rivers

We compiled 476 modern fluvial gradients (39–43), in addition to 30 modern alluvial fan gradients (39). Figure 4B in the main text shows the histograms of the fluvial gradients measured in modern rivers and alluvial fans along with the hypothesized natural depositional slope gap (39). In Figure 3D of the main text, we reproduced the ratio of slope and Froude number and the depth to width ratios reported in Parker (44) for modern braided, meandering, and straight channels.

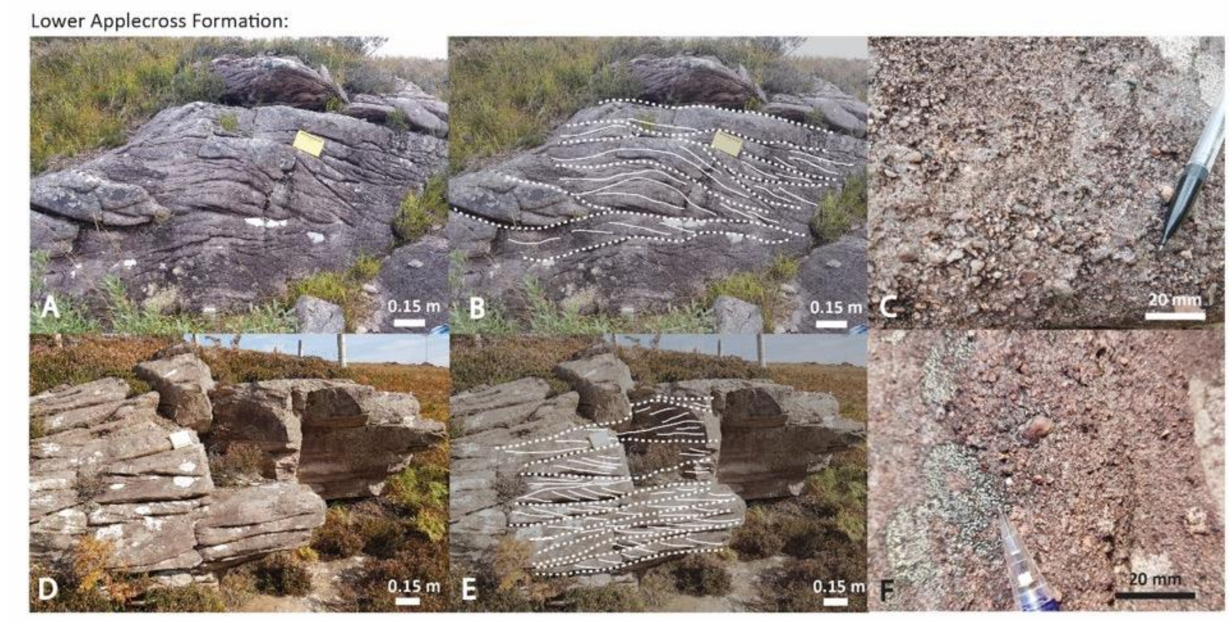

Fig. S1. Supplementary field photographs in the Lower Applecross. A, D) Original field photographs in the Lower Applecross. B, E) Annotated images where the dashed lines indicate the interpreted erosional boundaries and the solid lines indicate the observed cross-bedding. C, F) Representative macro photographs showing the grain-size observed at individual outcrops.

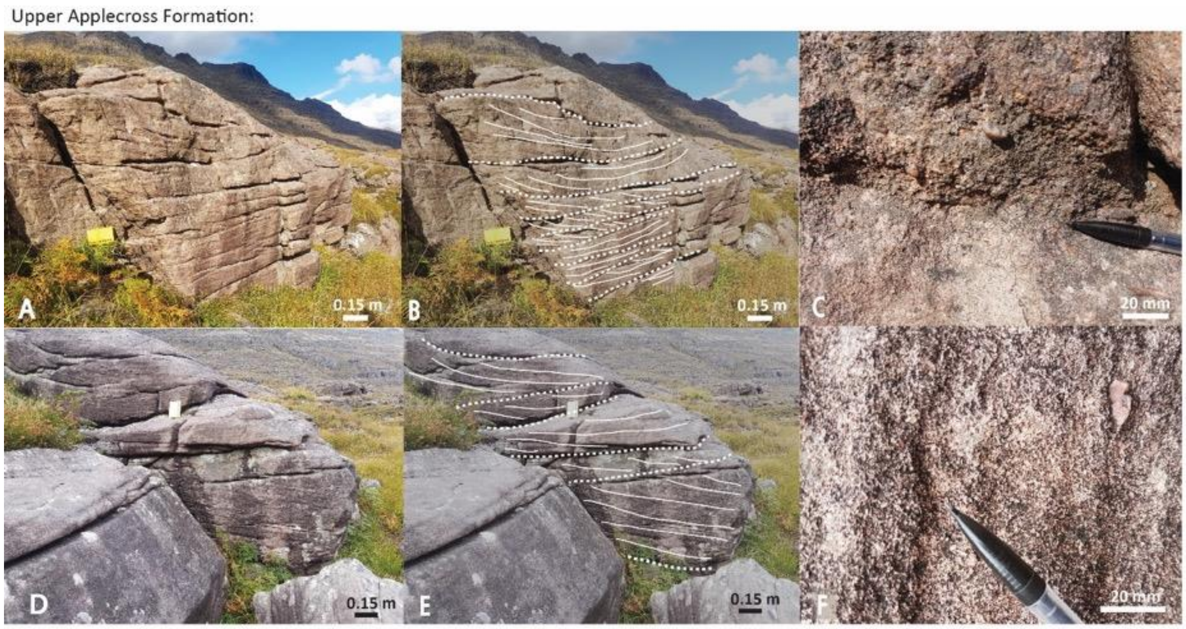

Fig. S2. Supplementary field photographs in the Upper Applecross. A, D) Original field photographs in the Upper Applecross. B, E) Annotated images where the dashed lines indicate the interpreted erosional boundaries and the solid lines indicate the observed cross-bedding. C, F) Representative macro photographs showing the grain-size observed at individual outcrops.

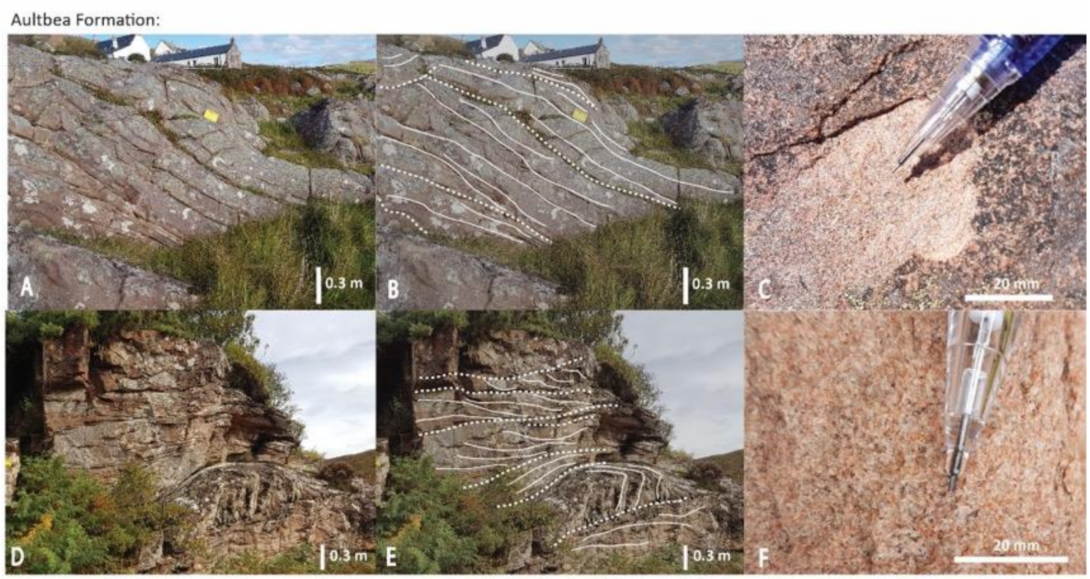

Fig. S3. Supplementary field photographs in the Aultbea Formation. A, D) Original field photographs in the Aultbea Formation. B, E) Annotated images where the dashed lines indicate the interpreted erosional boundaries and the solid lines indicate the observed cross-bedding. C, F) Representative macro photographs showing the grain-size observed at individual outcrops.

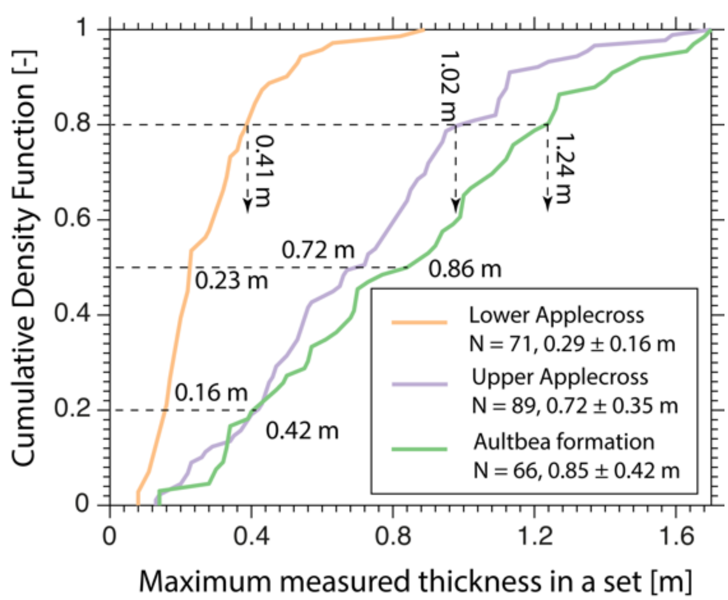

Fig. S4. Maximum set thickness measured within individual sets. Cumulative density function of the maximum set thickness measured within individual sets across the three stratigraphic sampling intervals. The dashed lines indicate 20^{th}, 50^{th}, and 80^{th} percentile of the maximum set thickness. The mean and standard deviation of the maximum set thickness is indicated in the figure legend. The increase in set thickness with stratigraphic height is evident not only in the bulk statistics of set thickness (Fig. 2G), but also in the measured maximum set thickness within individual sets across LAF, UAF, and Aultbea Formation.

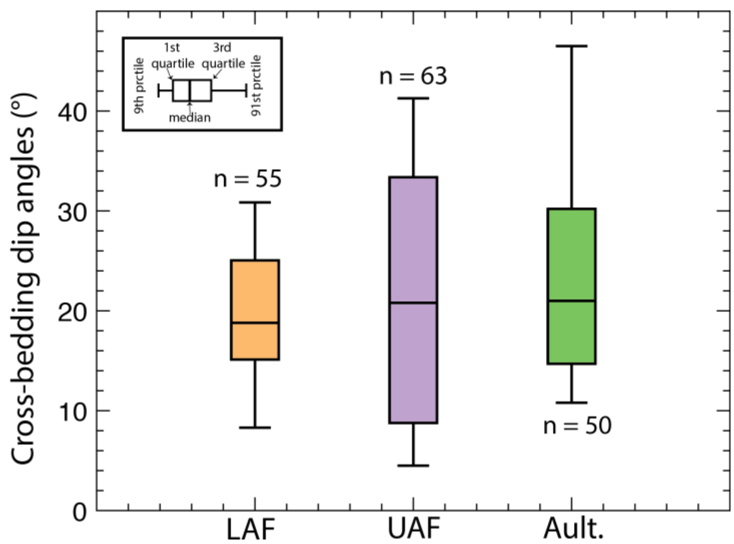

Fig. S5. Cross-bedding angles measured in the Torridonian Group. Boxplots of the measured cross-bedding angles, which were corrected for the depositional dip (orange – LAF; purple – UAF; green – Aultbea Formation). These dip angles are similar to modern lee-face angles of river dunes, and markedly shallower than the dip of the inferred lateral accretion surfaces (Figs. S6, S7).

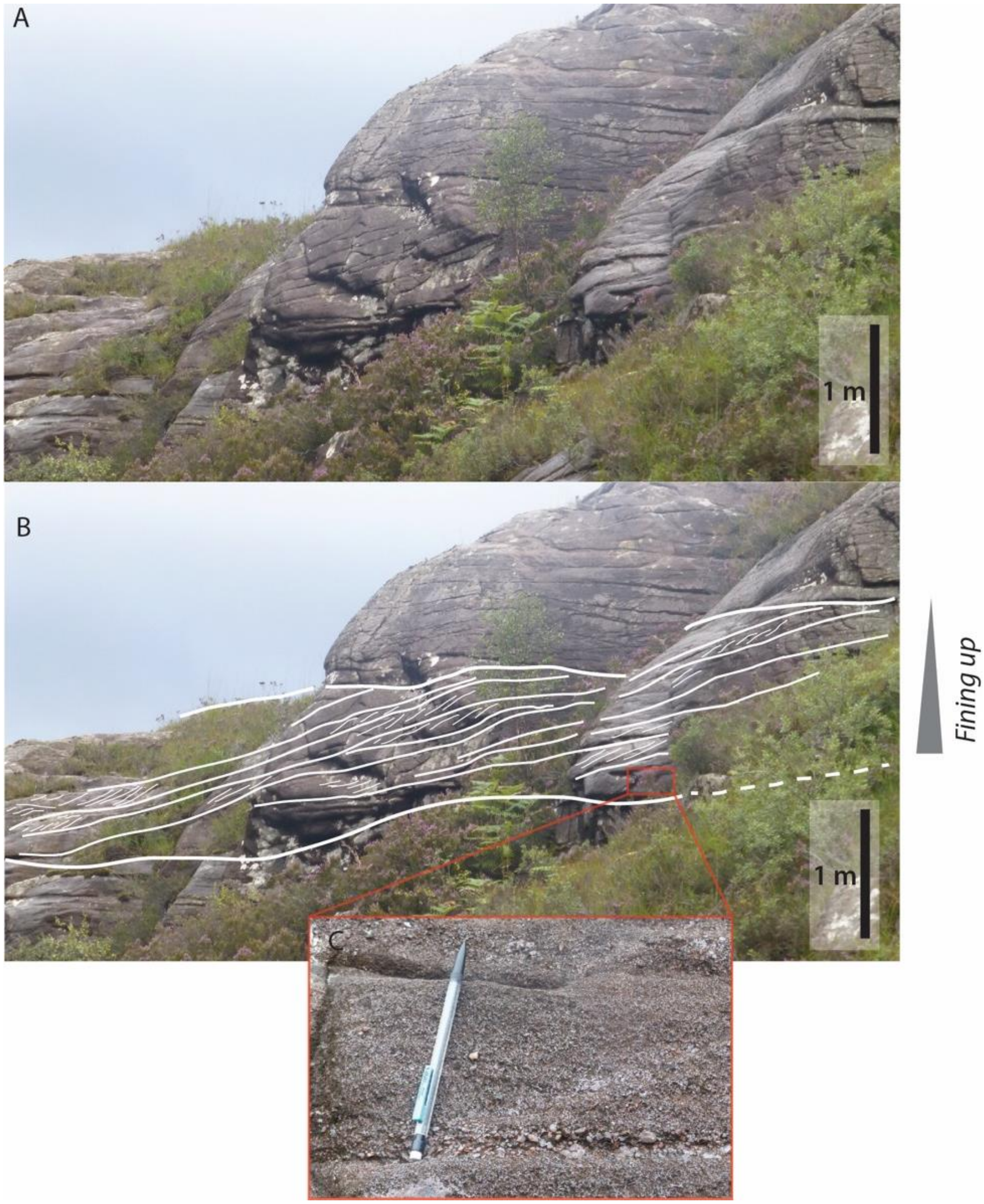
A
1 m
B
Fining up
1 m
C

Fig. S6. Rare preserved barform in the Lower Applecross. A) Uninterpreted and B) interpreted truncated barform outcrop photographs in the Lower Applecross (location coordinates: NG 95500 68702). The deposits are characterized by upward fining with the base of the major erosional surface composed of pebble lag (C). This coarse pebble lag is also a feature of the major erosional surface that bound the inferred lateral accretion sets. Solid, thick white lines indicate the lateral accretion surfaces and thin white lines indicate cross-stratification, which was inferred to represent superimposed bedforms on this putative barform. The maximum measured thickness of this truncated barform was 1.7 m.

Fig. S7. Rare preserved barform in the Upper Applecross. A) Uninterpreted and B) interpreted truncated barform outcrop photographs in the Upper Applecross (location coordinates: NG 91694 55653). Solid, thick white lines indicate the lateral accretion surfaces and thin white lines indicate cross-stratification, which was inferred to represent superimposed bedforms on this putative barform. The maximum measured thickness of this truncated barform was 4.7 m.

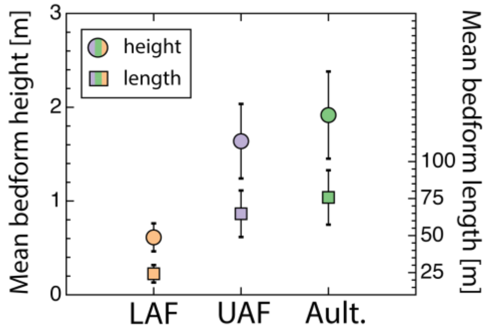

Fig. S8. Reconstructed geometry of bedforms in the Torridonian Sandstone. Reconstructed bedform heights using scaling of mean cross-set thickness and formative dune heights (left axis; circular markers). The bedform lengths were reconstructed using the empirical scaling relationship presented in Bradley and Venditti (15) (right axis; square markers).

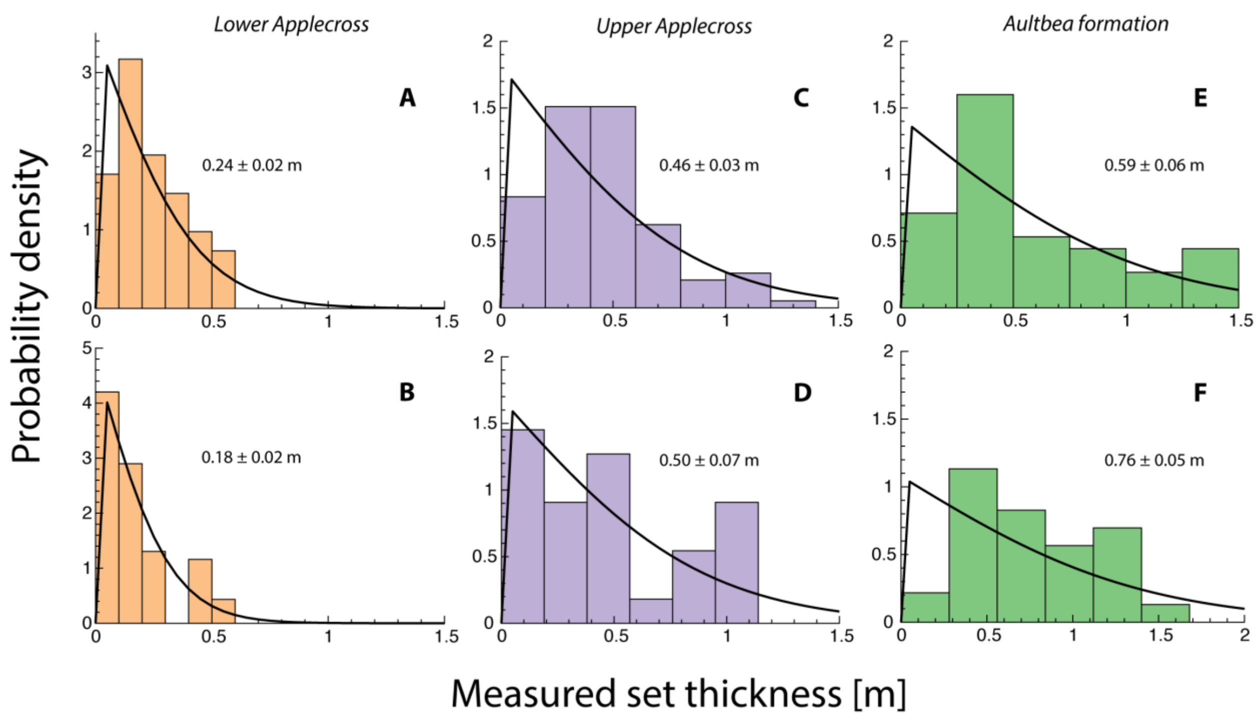

Fig. S9. Comparison of set thickness distribution with theory. Estimated probability density functions for measured set thicknesses where near-complete exposure of sets was available for (A-B) Lower Applecross, (C-D) Upper Applecross, and (E-F) Aultbea Formation. The solid black lines indicate the theoretical prediction (11) where the parameter *a* was estimated using $a = 1.64493/\langle d_{st} \rangle$.

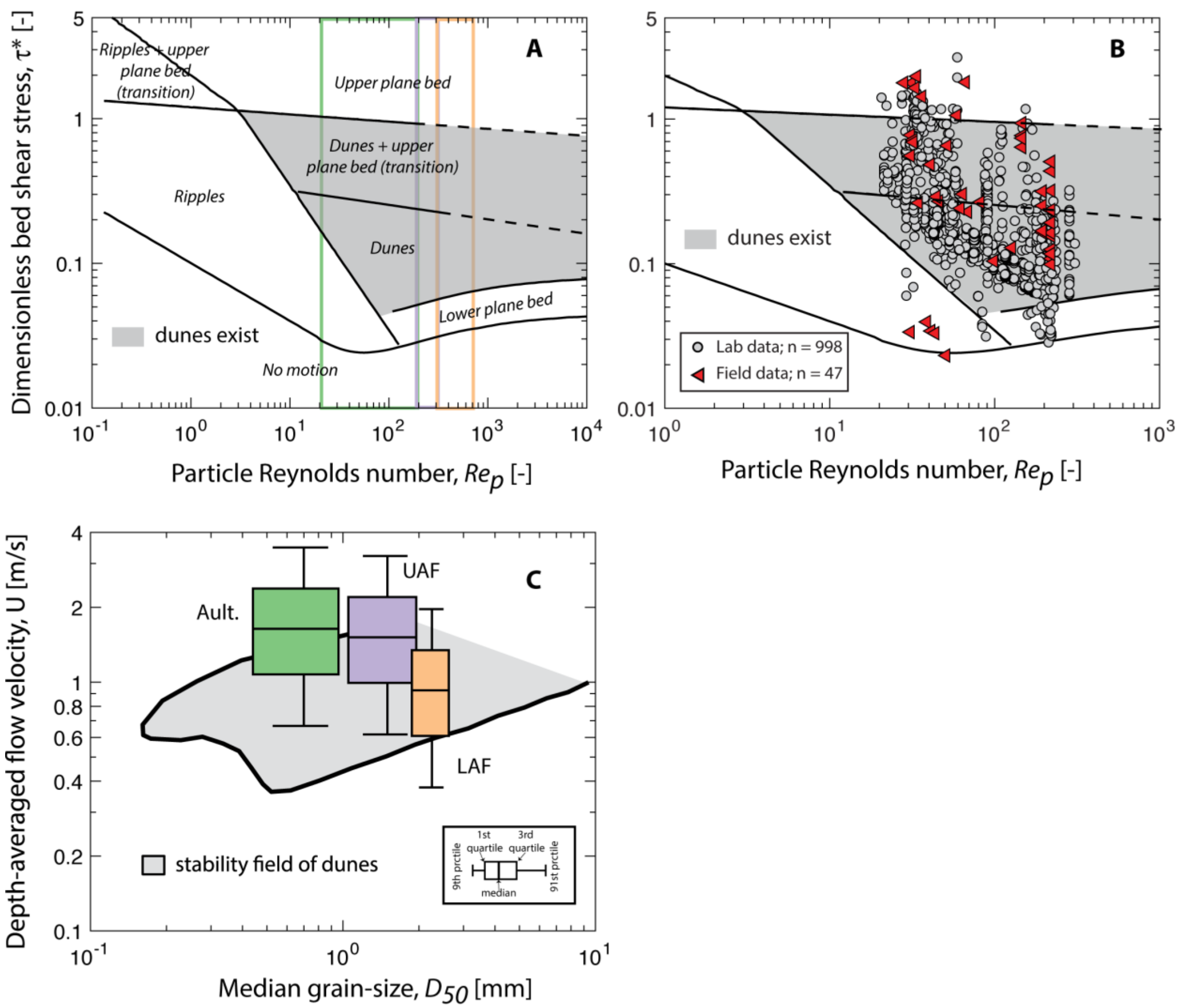

Fig. S10. Bedform stability diagram. A) Bedform stability diagram of Lamb et al. (20). The highlighted gray area indicates the stability field for the existence of river dunes. The estimated particle Reynolds number (equation S3C) for the three stratigraphic sampling intervals are indicated using colored rectangles. The solid black lines are fits of Lamb et al. (20) to the bedform transition boundaries validated using existing experimental or field studies. The dashed black lines denote the extrapolation of these bedform transition boundaries to higher particle

Reynolds numbers (20). B) Laboratory and field data with the same Re_p range as the Torridonian Sandstone. The solid gray markers are experimental data, and the red triangles are field data, which were derived from a recent global compilation (21). C) Bedform stability diagram expressed in terms of depth-averaged flow velocity and median grain-size (19), where the region bounded by the solid black line delineates the phase space for the stable existence of fluvial dunes. Estimated depth-averaged flow velocities using Monte Carlo sampling are also indicated (equation 5 in *Materials and Methods*).

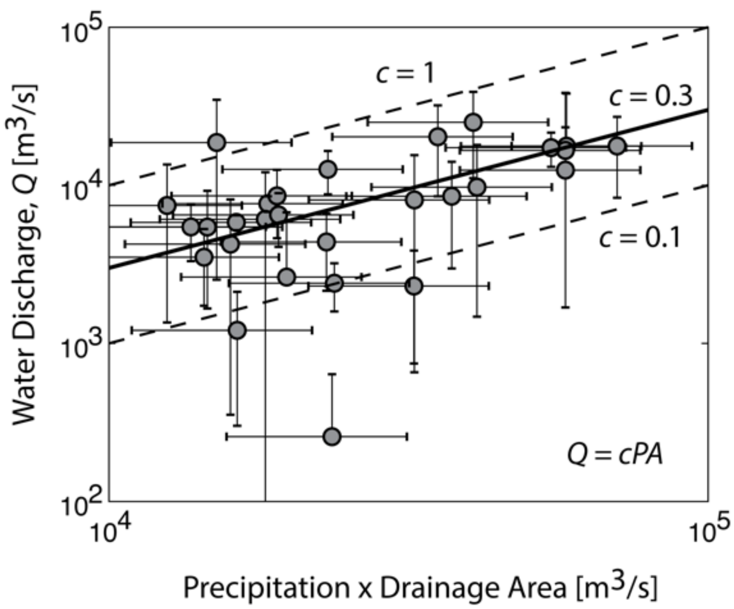

Fig. S11. Relationship between water discharge, precipitation rate, and drainage area in modern continental-scale rivers in subtropical and temperate regions. The mean and standard deviation of the observed water discharge are shown on the y-axis. The average period of record varies from station to station with a mean of 21.5 years (45). The product of monthly precipitation rate and drainage area are indicated on the y-axis. The markers indicate the computed value of PA for P = 0.75 m/yr, and the error bars show the extent of computed value for P = 0.5 m/yr and 1 m/yr.

This range corresponds to the observed global mean monthly precipitation rates in the subtropical and temperate regions (46).

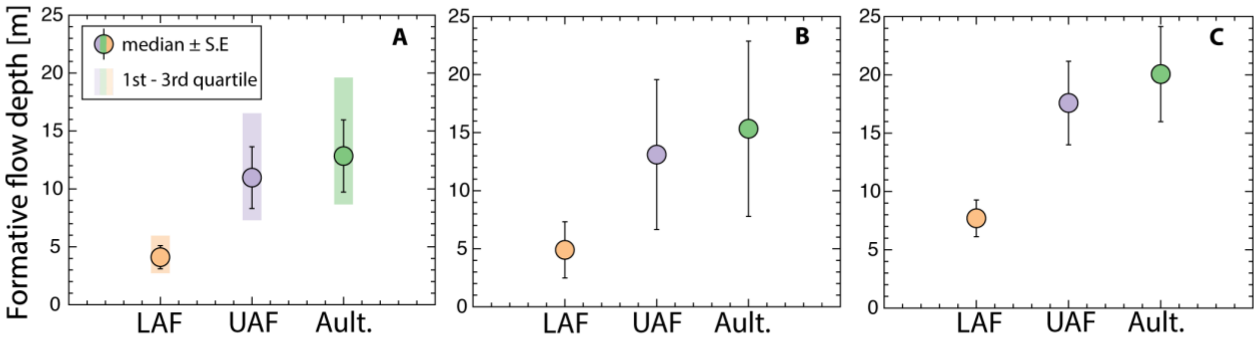

Fig. S12. Estimated flow depths for the Torridonian Group. A) Estimated *H* using the scaling relationship and the uncertainties of (15). B) Estimated *H* using the values of H/h_d reported in (10). C) Estimated *H* using equation (S2) proposed by Allen (17).

Table S1. Cross-set thickness and median grain-size measured in the Torridonian Group

Coordinates	Stratigraphic sampling interval	Mean cross-set thickness [m]	Number of measurements	Estimated median grain-size [mm]	Additional notes
NG 93150 78407	LAF	0.22	57	2.5; 1.5	7 sets observed. Bottom set was v. coarse sand to granules, and top 6 sets were coarse to v. coarse sand
NG 92715 70420	LAF	0.17	80	2.0; 3.0; 4.0	11 sets observed. Granules were typical of most sets. One set composed of fine gravel, and one set composed of granules

NG 76853 73710	LAF	0.14	97	2.0; 3.0	12 sets identified. All deposits were characterized by granules with some sets coarser with granules between 2 to 4 mm.
NG 79192 - 60530	LAF	0.66	10	2.0	v. coarse sand to granules
NC 22492 - 24866	LAF	0.24	41	1.5; 3.0; 0.8	bottom 3 sets were v. coarse sand, and one set was composed of granules. Top set was composed to medium to coarse sand
NC 22545 - 24814	LAF	0.17	69	1.5	v. coarse sand
NC 22552 - 24746	LAF	0.15	70	3.0; 2.5; 1.5	3 sets with overall upward fining trend. The grain size in sets ranged from granules and occasional pebbles to v. coarse sand

NC 15426 - 05634	LAF	0.41	26	2.5; 3.0; 2.5; 3.0; 2.5	v. coarse sand to granules with occasional pebbles
NC 15436 - 05600	LAF	0.26	57	2.5; 3.0; 2.5; 3.0; 2.5	v. coarse sand to granules with occasional pebbles
NG 95806 68529	LAF	0.28	12	3.0; 2.0; 1.5	3 sets with upward fining trend. Granules in bottom set and v. coarse sand in the top set
NG 95565 68685	LAF	0.23	8	1.0	Coarse sand
NG 95500 68702	LAF	0.22	10	1.0	Coarse sand
NG 95463 68727	LAF	0.27	7	1.3; 2.5	Stratigraphically higher set had 1 to 2 mm sediment sizes visible, but dominantly made up of sediment size close to 1 mm.

					Lowest set was composed of granules in the 2 to 3 mm range.
NG 95178 68806	LAF	0.26	9	1.5	Dominantly 1 to 2 mm with granules at the base of sets.
NG 77774 - 41846	UAF	0.70	9	1	Medium to coarse sand with grain size closer to 1 mm
NG 77778 - 41705	UAF	0.44	6	0.75	Observed grain size was between 0.5 and 1 mm
NG 77779 - 41641	UAF	0.84	11	0.5	Medium to coarse sand
NG 77727 - 41579	UAF	0.46	28	0.4	Medium sand and slightly finer than previous location
NG 77922 - 41565	UAF	0.67	15	0.4	Medium sand and slightly finer than NG 77779-41641 location sets

NG 91678 55533	UAF	0.80	42	2.5; 1.5; 0.75	6 sets were observed. Bottom set was v. coarse sand with pebbles. Higher 3 sets were coarse to v. coarse sand. The top 2 sets were medium to coarse sand, finer than 1 mm but coarser than 0.5 mm
NG 91653 55704	UAF	0.78	36	1.75; 1.5; 1	4 sets observed. The middle set was v.coarse sand. The bottom set was coarser than the middle set but still v. coarse sand. The top sets were coarse to v. coarse sand.

NG 91921 55947	UAF	0.79	25	0.75; 0.5; 1.5; 2	4 sets were interpreted with different grain-sizes. The sets were composed of v. coarse sand with pebbles, coarse to v. coarse sand, medium to coarse sand, and coarse to v. coarse sand
NG 91942 55960	UAF	0.42	30	2.5	5 sets were observed and all sets were composed of pebbles and coarse granules
NG 91901 55936	UAF	0.71	41	1; 0.5; 2.5; 1; 1; 1.5	6 sets observed with varying grain-sizes. We noted sets with coarse sand with some pebbles, medium to coarse sand, granules, and coarse sand

NG 91701 55534	UAF	0.49	29	3; 1.5; 1.5; 1.5; 2.5	5 sets were observed. One set was composed of granules, another set was composed of coarse to v. coarse sand with lenses of medium sand. Two sets were classified as v. coarse sand, and finally one set was v. coarse sand with granules > 2 mm.
NG 76832 43318	UAF	0.97	20	0.5	All 3 sets composed of medium sand
NG 76796 43296	UAF	0.42	30	0.5; 1; 2	4 sets observed with 2 sets composed of medium sand, one set composed of coarse sand and one set composed of v. coarse sand and pebbles

NB 98096 12863	UAF	0.45	96	1.5	8 sets observed and all composed of v. coarse sand
NB 97224 13317	UAF	0.52	39	1.5; 3.5; 3; 4	5 sets observed, which were much coarser than other UAF sets. Pebbles and granules were noted throughout the locality
NG 84374 91884	UAF	0.49	82	1.5	9 sets observed. All sets composed of v. coarse sand with occasional granules and pebbles
NG 84022 92369	UAF	0.40	63	1.5; 3; 1.5	8 sets were observed. All sets were composed of v. coarse sand except for one. That set was composed of granules and very fine gravel
NG 71230 39983	Ault.	0.79	48	0.5	Medium sand in all sets. 4 sets were observed

NG 71314 39873	Ault.	0.72	33	0.2	Fine to medium sand
NG 71024 37955	Ault.	0.58	45	0.2	5 sets composed of fine to medium sand
NG 71210 38192	Ault.	0.69	22	0.35	3 sets were identified.
NG 71024 37955	Ault.	0.43	32	0.2	Fine to medium sand
NG 71172 38779	Ault.	0.62	19	0.2	Fine to medium sand
NG 88706 94043	Ault.	0.45	31	0.2	Fine to medium sand
NG 88663 94099	Ault.	0.51	27	0.75; 1.25	3 sets were identified, and they were composed of medium to coarse sand, and coarse to v. coarse sand
NG 88774 94062	Ault.	0.62	36	0.75; 1; 0.2	4 sets were identified, and they were composed of coarse sand, and fine to medium sand

NB 98947 13842	Ault.	0.76	82	0.75; 0.2	9 sets were identified. 3 of them were composed of coarse sand, and the rest were composed of fine to medium sand
NB 99315 10309	Ault.	0.58	48	0.5	Medium sand
NB 99050 09933	Ault.	0.93	43	0.5	Medium sand
NG 88934 95450	Ault.	0.87	50	0.5; 0.25	Total of 4 sets were identified. 3 sets composed of medium sand, and one set composed of fine to medium sand
NG 85160 - 90783	Ault.	0.12	9	1.5; 2.5	Only instance in Aultbea formation where granules > 2 mm were documented
NG 89150 - 96078	Ault.	0.49	20	1.5	3 v. coarse sand sets

NG 89169-960568	Ault.	0.46	13	1; 1.5	Sets with coarse sand and v. coarse sand were documented
NG 89202 - 96095	Ault.	0.68	11	1; 1.5	v. coarse sand with occasional pebble/granule

Supplementary References

1. Peach BN, Horne J (1892) The Olennellus Zone in the north-west Highlands of Scotland. *Q J Geol Soc* 48(1888):227–242.
2. Allen P (1948) Wealden petrology : The Top Ashdown Pebble Bed and the Top Ashdown Sandstone. *Q J Geol Soc* 104(1–4):257 LP – 321.
3. Nicholson PG (1993) *A basin reappraisal of the Proterozoic Torridon Group, northwest Scotland* (International Association of Sedimentologists).
4. Stewart AD (2002) The later Proterozoic Torridonian rocks of Scotland: their sedimentology, geochemistry and origin. *Geological Society, London* (Geological Society of London), p 132.
5. Stewart AD (1969) Torridonian Rocks of Scotland Reviewed. *AAPG, Memoirs*, ed Kay M (American Association of Petroleum Geologists), pp 595–608.
6. Kinnaird TC, et al. (2007) The late Mesoproterozoic–early Neoproterozoic tectonostratigraphic evolution of NW Scotland: the Torridonian revisited. *J Geol Soc London* 164(3):541–551.
7. Turnbull MJM, Whitehouse MJ, Moorbath S (1996) New isotopic age determinations for the Torridonian, NW Scotland. *J Geol Soc London* 153(6):955–964.
8. Parnell J, Mark D, Fallick AE, Boyce A, Thackrey S (2011) The age of the Mesoproterozoic Stoer Group sedimentary and impact deposits, NW Scotland. *J Geol Soc London* 168(2):349–358.
9. Cardozo N, Allmendinger RW (2013) Spherical projections with OSXStereonet. *Comput Geosci* 51:193–205.
10. Leclair SF, Bridge JS (2001) Quantitative Interpretation of Sedimentary Structures Formed by River Dunes. *J Sediment Res* 71(5):713–716.
11. Paola C, Borgman L (1991) Reconstructing random topography from preserved stratification. *Sedimentology* 38(4):553–565.
12. Ganti V, Paola C, Foufoula-Georgiou E, Foufoula-Georgiou E (2013) Kinematic controls on the geometry of the preserved cross sets. *J Geophys Res Earth Surf* 118(3):1296–1307.
13. Reesink AJHH, et al. (2015) Extremes in dune preservation: Controls on the completeness of fluvial deposits. *Earth-Science Rev* 150:652–665.
14. Bridge JS (1997) Thickness of sets of cross strata and planar strata as a function of formative bed-wave geometry and migration, and aggradation rate. *Geology* 25(11):971–974.
15. Bradley RW, Venditti JG (2017) Reevaluating dune scaling relations. *Earth-Science Rev* 165:356–376.
16. Yalin MS (1964) Geometrical properties of sand waves. *J Hydraul Div* 90(5):105–119.
17. Allen JRL (1968) *Current Ripples* (North-Holland Publishing Co., Amsterdam).
18. Southard JB, Boguchwal LA (1990) Bed configuration in steady unidirectional water flows; Part 2, Synthesis of flume data. *J Sediment Res* 60(5):658–679.
19. Carling PA (1999) Subaqueous gravel dunes. *J Sediment Res* 69(3):534–545.
20. Lamb MP, Grotzinger JP, Southard JB, Tosca NJ (2012) Were Aqueous Ripples on Mars Formed by Flowing Brines? *Sedimentary Geology of Mars*, eds Grotzinger JP, Milliken RE (SEPM Society for

Sedimentary Geology). Available at: https://doi.org/10.2110/pec.12.102.0139.
21. Ohata K, Naruse H, Yokokawa M, Viparelli E (2017) New Bedform Phase Diagrams and Discriminant Functions for Formative Conditions of Bedforms in Open-Channel Flows. *J Geophys Res Earth Surf* 122(11):2139–2158.
22. Allen JRL (1984) *Sedimentary Structures; Their Character and Physical Basis* (Elsevier, Amsterdam).
23. Southard JB (1991) Experimental Determination of Bed-Form Stability. *Annu Rev Earth Planet Sci* 19(1):423–455.
24. Mukhopadhyay S, Choudhuri A, Samanta P, Sarkar S, Bose PK (2014) Were the hydraulic parameters of Precambrian rivers different? *J Asian Earth Sci* 91:289–297.
25. Van der Neut M, Eriksson PG (1999) Palaeohydrological parameters of a Proterozoic braided fluvial system (Wilgerivier Formation, Waterberg Group, South Africa) compared with a Phanerozoic example. *IAS Spec Publ* 28:381–392.
26. Eriksson PG, Bumby AJ, Brümer JJ, van der Neut M (2006) Precambrian fluvial deposits: Enigmatic palaeohydrological data from the c. 2–1.9 Ga Waterberg Group, South Africa. *Sediment Geol* 190(1):25–46.
27. Eriksson P, et al. (2008) Palaeohydrological data from the c. 2.0 to 1.8 Ga Waterberg Group, South Africa: discussion of a possibly unique Palaeoproterozoic fluvial style. *South African J Geol* 111(2–3):281–304.
28. Köykkä J (2011) Precambrian alluvial fan and braidplain sedimentation patterns: Example from the Mesoproterozoic Rjukan Rift Basin, southern Norway. *Sediment Geol* 234(1–4):89–108.
29. Köykkä J (2011) The sedimentation and paleohydrology of the Mesoproterozoic stream deposits in a strike-slip basin (Svinsaga Formation), Telemark, southern Norway. *Sediment Geol* 236(3–4):239–255.
30. Sarkar S, Samanta P, Mukhopadhyay S, Bose PK (2012) Stratigraphic architecture of the Sonia Fluvial interval, India in its Precambrian context. *Precambrian Res* 214–215:210–226.
31. Eriksson PG, Bose PK, Catuneanu O, Sarkar S, Banerjee S (2008) Precambrian clastic epeiric embayments: examples from South Africa and India. *Dyn epeiric seas* 48:119–136.
32. Rainbird RH (1992) Anatomy of a large-scale braid-plain quartzarenite from the Neoproterozoic Shaler Group, Victoria Island, Northwest Territories, Canada. *Can J Earth Sci* 29(12):2537–2550.
33. Köykkä J (2011) Precambrian alluvial fan and braidplain sedimentation patterns: Example from the Mesoproterozoic Rjukan Rift Basin, southern Norway. *Sediment Geol* 234(1–4):89–108.
34. Köykkä J (2011) The sedimentation and paleohydrology of the Mesoproterozoic stream deposits in a strike-slip basin (Svinsaga Formation), Telemark, southern Norway. *Sediment Geol* 236(3–4):239–255.
35. Sarkar S, Samanta P, Mukhopadhyay S, Bose PK (2012) Stratigraphic architecture of the Sonia Fluvial interval, India in its Precambrian context. *Precambrian Res* 214–215:210–226.
36. Eriksson PG, Bumby AJ, Brümer JJ, van der Neut M (2006) Precambrian fluvial deposits: Enigmatic palaeohydrological data from the c. 2–1.9 Ga Waterberg Group, South Africa. *Sediment Geol* 190(1):25–46.
37. Schumm SA (1968) *River Adjustment to Altered Hydrologic Regimen- Murrumbidgee River and Paleochannels, Australia* (US Government Printing Office).
38. Schumm SA (1972) Fluvial Paleochannels. *Sepm*, eds Rigby JK, Hamblin WK (SEPM Society for Sedimentary Geology), pp 98–107.
39. Blair TC, McPherson JG (1994) Alluvial fans and their natural distinction from rivers based on morphology, hydraulic processes, sedimentary processes, and facies assemblages. *J Sediment Res* 64(3a):450–489.
40. Trampush SM, Huzurbazar S, McElroy B (2014) Empirical assessment of theory for bankfull characteristics of alluvial channels. *Water Resour Res* 50(12):9211–9220.
41. Gaurav K, et al. (2015) Morphology of the Kosi megafan channels. *Earth Surf Dyn* 3(3):321–331.
42. Métivier F, et al. (2016) Geometry of meandering and braided gravel-bed threads from the Bayanbulak Grassland, Tianshan, P. R. China. *Earth Surf Dynam* 4(1):273–283.
43. Chatanantavet P, Lamb MP, Nittrouer JA (2012) Backwater controls of avulsion location on deltas. *Geophys Res Lett* 39(1). doi:10.1029/2011GL050197.
44. Parker G (1976) On the cause and characteristic scales of meandering and braiding in rivers. *J Fluid Mech* 76(3):457–480.
45. VOROSMARTY CJ, FEKETE BM, TUCKER BA (1998) Global River Discharge, 1807-1991, V[ersion]. 1.1 (RivDIS). doi:10.3334/ornldaac/199.
46. Macdonald FA, Swanson-Hysell NL, Park Y, Lisiecki L, Jagoutz O (2019) Arc-continent collisions in the tropics set Earth's climate state. *Science* 364:181–184.